DØ Note 6006-CONF

# Search for Higgs boson production in dilepton plus missing transverse energy final states with 5.4 fb$^{-1}$ of $p\overline{p}$ Collisions at $\sqrt{s} = 1.96$ TeV

The DØ Collaboration
*URL http://www-d0.fnal.gov*
(Dated: November 16, 2009)

A search for the standard model (SM) Higgs boson is presented using a sample of dilepton events with large missing transverse momentum extracted from 5.4 fb$^{-1}$ of $p\overline{p}$ collisions at $\sqrt{s} = 1.96$ TeV. Final states containing either $e^+e^-$, $e^\pm\mu^\mp$, or $\mu^+\mu^-$ are considered. The data sample used in this analysis was collected between April 2002 and June 2009 with the DØ detector during Run II of the Fermilab Tevatron collider. No significant excess above background estimations is observed, and upper limits on Higgs boson production are derived, which are 1.5 times the expected SM cross section at 95% confidence level for a Higgs boson mass of $M_H$=165 GeV.

*Preliminary Results for Fall Conferences 2009*

## I. INTRODUCTION

In the standard model (SM) the masses of the charged fermions are generated by their interaction with a scalar field, the Higgs boson, which has yet to be observed experimentally. The Higgs boson represents the residual degree of freedom after the spontaneous symmetry breaking of the electroweak gauge symmetry $\mathcal{SU}(2) \otimes \mathcal{U}(1)$ which is responsible for the generation of the masses of the $W$ and $Z$ bosons. Direct searches at the CERN $e^+e^-$ collider (LEP) yield a lower limit for the SM Higgs boson mass, $M_H > 114.4$ GeV [1] at 95% confidence level (C.L.). Indirect measurements via fits to the electroweak precision data give an upper bound of $M_H < 186$ GeV [2] at 95% C.L. when combined with the direct searches.

In this note we present a search for the Higgs boson in final states containing two reconstructed leptons and missing transverse energy ($\not\!\!E_T$), using data collected with the DØ detector at the Fermilab Tevatron corresponding to an integrated luminosity of 5.4 fb$^{-1}$. We consider final states containing either two reconstructed electrons, $e^+e^-$, an electron and a muon, $e^\pm\mu^\mp$, or two muons, $\mu^+\mu^-$. Final states with tau leptons are detected through the tau leptonic decay modes to electrons or muons, or final states which leave an electron-like signal in the detector. Together these final states provide the largest sensitivity for the SM Higgs boson at the Tevatron for $M_H \approx 160$ GeV [3, 4]. The search presented in this note considers not only the contribution to the dilepton plus $\not\!\!E_T$ final state from the $H \to WW^{(*)} \to \ell\ell'\nu\nu$ ($\ell, \ell' = e, \mu, \tau$) decay where the Higgs boson is produced through the gluon fusion process, but also contributions from the weak boson fusion process. In addition we also consider final states originating from Higgs boson production in association with a vector boson ($WH$ or $ZH$), where leptons may originate from the vector boson or Higgs boson decay. Results are presented relative to the sum of the SM predictions for the cross sections of the different Higgs boson production processes, assuming the SM values for the Higgs branching fractions. The limits on Higgs boson production obtained in this analysis supersede previous DØ results presented in [5, 6].

## II. DØ DETECTOR

We briefly describe the main components of the DØ Run II detector [7] relevant to this analysis. The central tracking system consists of a silicon microstrip tracker (SMT) and a central fiber tracker (CFT), both located within a 2 T axial magnetic field. The SMT strips have a typical pitch of 50–80 $\mu$m, and the design is optimized for tracking and vertexing over the pseudorapidity range $|\eta| < 3$, where $\eta = -\ln(\tan\theta/2)$ with $\theta$ being the polar angle relative to the proton beam direction. The system has a six-barrel longitudinal structure, with each barrel a set of four silicon layers arranged axially around the beam pipe, interspersed with sixteen radial disks. In addition, a new layer of silicon (Layer 0) was added just outside the beam pipe in 2006. The CFT has eight thin coaxial barrels, each supporting two doublets of overlapping scintillating fibers of 0.835 mm diameter, one doublet parallel to the beam axis, the other alternating by $\pm 3^\circ$ relative to the beam axis.

A liquid-argon/uranium calorimeter surrounds the central tracking system and consists of a central calorimeter (CC) covering to $|\eta| \approx 1.1$, and two end calorimeters (EC) extending coverage for $|\eta| < 4.2$, each housed in separate cryostats. Scintillators between the CC and EC cryostats provide sampling of showers for $1.1 < |\eta| < 1.4$.

The muon system is located outside the calorimeters and consists of a layer of tracking detectors and scintillation trigger counters inside toroid magnets which provide a 1.8 T magnetic field, followed by two similar layers behind each toroid. Tracking in the muon system for $|\eta| < 1$ relies on 10 cm wide drift tubes, while 1 cm mini-drift tubes are used for $1 < |\eta| < 2$.

Trigger and data acquisition systems are designed to accommodate the high luminosities of Run II. Based on preliminary information from tracking, calorimetry, and muon systems, the output of the first level of the trigger is used to limit the rate for accepted events to $\approx 1.5$ kHz. At the next trigger stage, with more refined information, the rate is reduced further to $\approx 0.8$ kHz. These first two levels of triggering rely mainly on hardware and firmware. The third and final level of the trigger, with access to all the event information, uses software algorithms and a computing farm, and reduces the output rate to $\approx 100$ Hz, which is written to tape.

## III. DATA AND MONTE CARLO SAMPLES

The data sample used in this analysis was collected between April 2002 and June 2009 (Run II) by the DØ detector at the Fermilab Tevatron collider at $\sqrt{s} = 1.96$ TeV, and corresponds to an integrated luminosity of 5.4 fb$^{-1}$ for the $e^\pm\mu^\mp$, $e^+e^-$, and $\mu^+\mu^-$ final states. The luminosity is measured with an accuracy of 6.1% using plastic scintillator arrays located in front of the EC cryostats, covering $2.7 < |\eta| < 4.4$ [8]. As an independent test the integrated luminosity is estimated by comparing the number of expected events in Monte Carlo (MC) using the NNLO $Z/\gamma^* \to ee$ ($\mu\mu$) cross

section to the number of observed events in the mass region 60< $M_{\ell\ell}$ <130 GeV. All known corrections are applied to the MC in order to reproduce the efficiencies measured in data. For the $e^{\pm}\mu^{\mp}$ final state the entire $M_{e\mu}$ spectrum is used considering the effect of the $\tau$ branching ratios to electrons and muons. The yield of Z candidates observed in data is consistent with the measurement of the luminosity within 5%.

Signal and SM background processes are simulated with PYTHIA [9] or ALPGEN [10] using the CTEQ6L1 [11] parton distribution functions (PDF), followed by a detailed GEANT-based [12] simulation of the DØ detector. Various Higgs boson production channels contribute to the total signal. The main production channel is the gluon fusion process $gg \to H \to WW^* \to \ell\nu\ell\nu$, followed by the the vector–boson fusion process (VBF) $q\bar{q} \to q\bar{q}H \to q\bar{q}WW^* \to q\bar{q}\ell\nu\ell\nu$. Smaller additional signal contributions come from $ZH$ and $WH$ production. The signal cross sections are normalized to NNLO calculations [13–16] (NLO calculations in the case of the vector boson fusion process) and the distribution of the transverse momentum of the Higgs boson generated in the gluon fusion process is reweighted to match the SHERPA simulation [18].

The main background processes for this analysis are diboson production, $Z$ decays in leptonic final states, electroweak $W$ + jet/$\gamma$ production, $t\bar{t}$ decays and multijet production with misidentified leptons. For the W(+jets) and Z(+jets) backgrounds we use the ALPGEN [10] event generator. The background MC samples for inclusive W and Z production are normalized using the NNLO cross sections calculations of [19] using the NLO CTEQ 6.1 PDF. The $Z$ boson $p_{\mathrm{T}}$ distribution is modeled to match the distribution observed in data [20], taking also into account the dependence on the number of reconstructed jets. To reproduce the $W$ $p_{\mathrm{T}}$ distribution in simulated events, the product of the measured $Z$ boson $p_{\mathrm{T}}$ spectrum in Ref. [20] multiplied by the ratio of $W$ to $Z$ boson $p_{\mathrm{T}}$ distributions at NLO from Ref. [21] is used to reweight events. The NNLO calculations of [22] are used for $t\bar{t}$ production, while the NLO $WW$, $WZ$ and $ZZ$ production cross section values are taken from [23]. For the main source of background, WW production, the $p_{\mathrm{T}}$ of the diboson system is modeled using the MC@NLO simulation [17] and the distribution of the opening angle of the two leptons is corrected to take into account the contribution from gluon fusion [24].

The background due to multijet production, when jets are misidentified as leptons, is determined from data. A sample of like-sign dilepton events is used in the $\mu\mu$ channel, corrected for like-sign contributions from other processes. The other channels use events with inverted lepton quality cuts, corrected to match the normalization and kinematics determined in the like-sign data.

## IV. EVENT SELECTION

The $H \to WW^{(*)} \to \ell\ell'$ ($\ell, \ell' = e, \mu, \tau$) candidates are selected by triggering on single or dilepton events using a three level trigger system. The first trigger level uses custom built hardware to select electron candidates based on energy deposition in the electromagnetic part of the calorimeter and muon candidates formed by hits in the muon system. The muon trigger requires in addition a high $p_{\mathrm{T}}$ central track reconstructed in the CFT by the specialized central track trigger (CTT). Digital signal processors in the second trigger level form muon track candidate segments defined by hits in the muon drift chambers and scintillators, and match lepton candidates to a more precise central track using additional SMT hits reconstructed by the silicon track trigger. At the third level, software algorithms running on a computing farm and exploiting the full event information are used to make the final selection of events which are recorded.

In the offline analysis, electrons are identified using calorimeter and tracking information. Electromagnetic showers are identified in the calorimeter by comparing the longitudinal and transverse shower profiles to those of simulated electrons. The showers must be isolated, deposit most of their energy in the electromagnetic part of the calorimeter, and pass a likelihood criterion that includes a spatial track match and, in the central detector region, an $E/p$ requirement, where $E$ is the energy of the calorimeter cluster and $p$ is the momentum of the track. Electrons must be reconstructed within a detector pseudorapidity $|\eta| < 2.0$ (2.5 in the $e\mu$ channel) and neglecting the region between the CC and EC cryostats, excluding electrons in $1.1 < |\eta| < 1.4$. The transverse momentum measurement of the electrons is based on calorimeter cell energy information.

Muon tracks are reconstructed from hits in the wire chambers and scintillators in the muon system and must match a track in the central tracker. To select isolated muons, the scalar sum of the transverse momentum of all tracks, other than that of the muon, in a cone of $\mathcal{R} = 0.5$ around the muon track is calculated, where $\mathcal{R} = \sqrt{(\Delta\phi)^2 + (\Delta\eta)^2}$ and $\phi$ is the azimuthal angle. The transverse energy deposited in the calorimeter in a hollow cone of $0.1 < \mathcal{R} < 0.4$ around the muon is also measured. In the $e\mu$ final state, both quantities are required to be $< 0.15 \times p_{\mathrm{T}}^{\mu}$, where $p_{\mathrm{T}}^{\mu}$ is the transverse momentum of the muon. In the $\mu\mu$ final state, the sum of the variables is required to be $< 0.4$ (0.5) $\times p_{\mathrm{T}}^{\mu}$ for the leading (trailing) muon. Muons are restricted to the fiducial coverage of the muon system $|\eta| < 2.0$. Muons from cosmic rays are rejected by requiring a timing criterion on the hits in the scintillator layers as well as applying restrictions on the distance of closes approach of the muon track to the selected primary vertex.

In all final states, two leptons originating from the same primary vertex are required to be of opposite charge.

Muons must have $p_T^\mu > 10$ GeV whereas electrons are required to have $p_{\rm T}^e > 15$ GeV. In the $\mu\mu$ final state one of the two muons is required to have $p_{\rm T}^\mu > 20$ GeV. Both muons must be separated from the nearest jet by $\Delta\mathcal{R} > 0.1$. In addition, in all three channels the dilepton invariant mass is required to exceed 15 GeV. This stage of the analysis is referred to as "pre-selection".

At this stage, the background is dominated by $Z/\gamma^*$ production. $Z/\gamma^*$ boson and multijet events are rejected with a cut on the opening angle $\Delta\phi_{\ell\ell}$, since most of the background decays are back-to-back. This is not the case for Higgs boson decays because of the spin correlations from the scalar decay. The opening angle $\Delta\phi_{\ell\ell}$ is required to be less than 2.0 radians.

The $Z/\gamma^*$ background is further suppressed by requiring missing transverse energy $\not\!\!E_T > 20$ GeV (in the $ee$ and $e\mu$ channels), or $\not\!\!E_T > 25$ GeV (in the $\mu\mu$ channel). In the $ee$ and $e\mu$ channels, events are further removed if the $\not\!\!E_T$ could have been produced by a mis-measurement of jet energies. A scaled $\not\!\!E_T$ variable, $\not\!\!E_T^{\rm Scaled}$, is used for this purpose. The jet transverse energy resolution is approximated by $\Delta E^{\rm jet} \cdot \sin\theta^{\rm jet}$ where $\Delta E^{\rm jet}$ is proportional to $\sqrt{E^{\rm jet}}$. The opening angle $\Delta\phi\,({\rm jet}, \not\!\!E_T\,)$ between this projected energy fluctuation and the missing transverse energy provides a measure of the contribution of the jet to the missing transverse energy. The scaled missing transverse energy is defined as:

$$\not\!\!E_T^{\rm Scaled} = \frac{\not\!\!E_T}{\sqrt{\sum_{\rm jets} \left(\Delta E^{\rm jet} \cdot \sin\theta^{\rm jet} \cdot \cos\Delta\phi\,({\rm jet}, \not\!\!E_T\,)\right)^2}}. \quad (1)$$

To suppress background where $\not\!\!E_T$ is coming from mis-measured lepton energy we apply a requirement on the minimal transverse mass $M_T^{\rm min}$, which is the the smallest of the two transverse masses $M_T$ built out of the momentum of either of the two leptons and $\not\!\!E_T$, with $M_T$ defined as

$$M_T(l, \not\!\!E_T\,) = \sqrt{2 p_T^l \not\!\!E_T\,(1 - \cos\Delta\phi(l, \not\!\!E_T\,))}. \quad (2)$$

$M_T^{\rm min}$ is required to be larger than 30 GeV in the $ee$ channel and larger than 20 GeV in the $e\mu$ and $\mu\mu$ channels. Table I shows the selection criteria used for the three different channels. Figure 1 shows the dilepton invariant mass and $\not\!\!E_T$ distributions in data, backgrounds, and signal at the pre-selection level for all three channels. The left column of Figure 2 shows the $\Delta\phi(\ell,\ell)$ distribution after the final selection for all three channels. Additional control plots can be found in Sec. A. As can be seen, the data are in good agreement with the expected background. Table II shows the number of expected and observed events after pre-selection and final selections for all three channels.

| Final state | | $e\mu$ | $ee$ | $\mu\mu$ |
|---|---|---|---|---|
| Cut 0 | Pre-selection | lepton ID, leptons with opposite charge and $p_T^\mu > 10$ GeV and $p_T^e > 15$ GeV invariant mass $M_{\ell\ell} > 15$ GeV $\mu\mu$: $\Delta\mathcal{R}(\mu, {\rm jet}) > 0.1$ and $p_T^\mu > 20$ GeV for the leading $\mu$ | | |
| Cut 1 | $\Delta\phi(\ell,\ell)$ (rad) | $< 2.0$ | $< 2.0$ | $< 2.0$ |
| Cut 2 | Missing Transverse Energy $\not\!\!E_T$ (GeV) | $> 20$ | $> 20$ | $> 25$ |
| Cut 3 | $\not\!\!E_T^{\rm Scaled}$ | $> 6$ | $> 6$ | |
| Cut 4 | $M_T^{min}$ $(\ell, \not\!\!E_T\,)$ (GeV) | $> 20$ | $> 30$ | $> 20$ |

TABLE I: Summary of the selection criteria for the three final states (blank entries indicate that no requirement is applied on that quantity for the specific channel).

## V. MULTIVARIATE DISCRIMINANTS

To improve the separation of signal from background, an artificial neural network (NN) is used in each of the three dilepton channels. The NNs were trained using approximately half of the background and signal events, the rest being

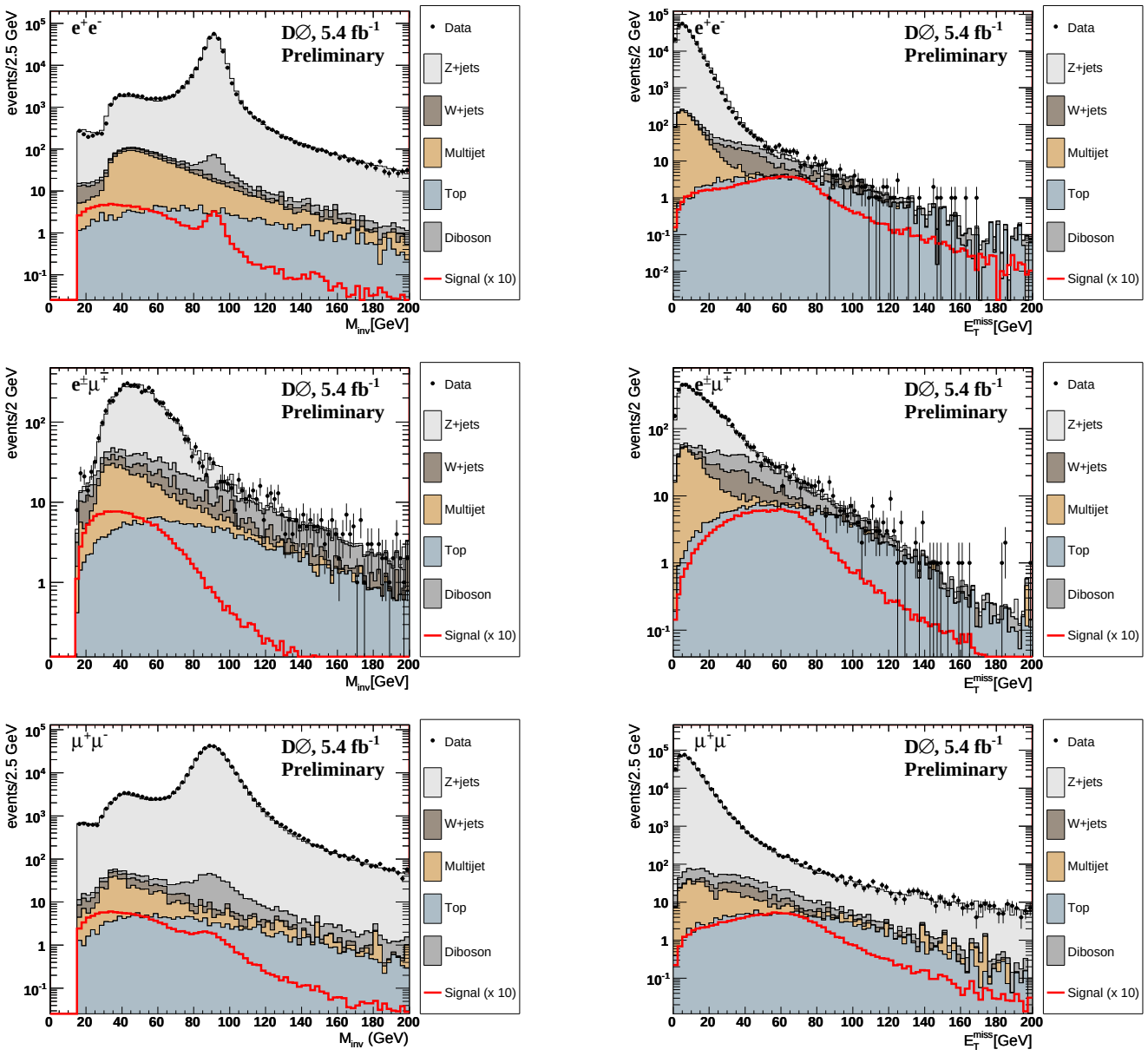


FIG. 1: Distributions of $\ell^+\ell^-$ mass (left) and $\not\!\!E_T$ (right) for data (points with error bars), background simulation (histograms, complemented with the QCD expectation) and signal expectation times 10 for $M_H = 165$ GeV (solid line) for the three channels separately after preselection.

used to test the networks' performance and to compare with data. A separate NN is trained for each Higgs boson mass tested. A weighted sum of all backgrounds was used during training.

A list of input variables was derived based on their separation power for each of the three channels. Those variables can be divided into three classes, lepton variables, event kinematics and angular variables. One of the input variables is a the lepton quality ranking, the minimum of the reconstruction quality $q$ of either of the two leptons. The quality depends on the reconstruction algorithm and is a likelihood probability for electrons and for the muons it is based on number of hits and layers in the muon system.

The NN input variables for the three channels are listed in Table III. The NN is applied to all events passing the final selection requirements described in Section IV. All the NN input variables show agreement between the sum of the MC backgrounds and the data after the selection cuts. The NN output for $m_{\rm H} = 165$ GeV is displayed in the right column of Figure 2 for all three channels.

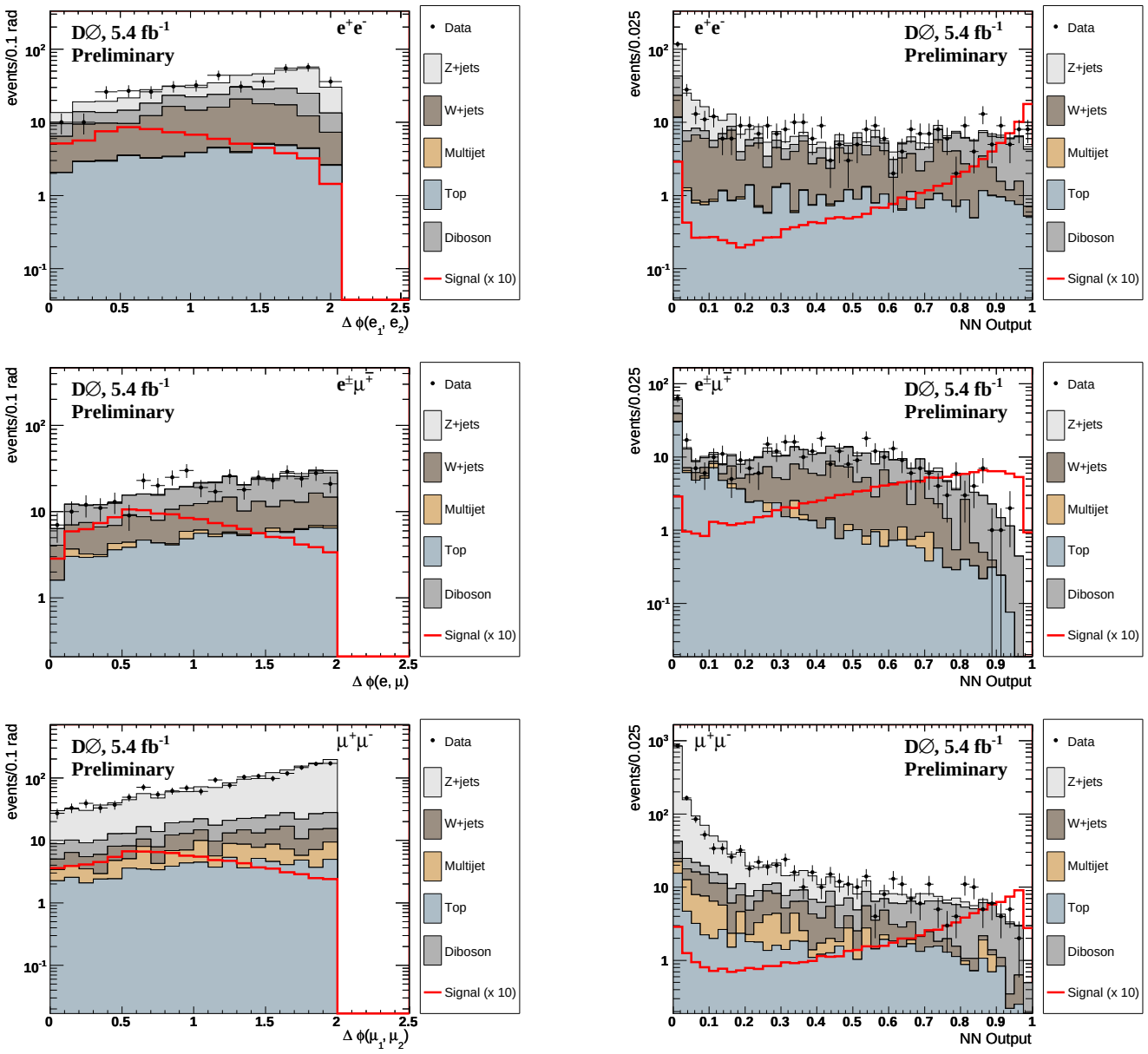


FIG. 2: Distribution of $\Delta\phi(\ell^+,\ell^-)$ and the neural net output variable after all selection criteria are applied (right) for data (points with error bars), background simulation (histograms, complemented with the QCD expectation) and signal expectation times 10 for $M_H = 165$ GeV (solid line) for the three channels separately.

| | $e\mu$ pre-selection | $e\mu$ final | $ee$ pre-selection | $ee$ final | $\mu\mu$ pre-selection | $\mu\mu$ final |
|---|---|---|---|---|---|---|
| $Z \to ee$ | $119.6 \pm 2.0$ | $0.0 \pm 0.0$ | $274886 \pm 105.5$ | $158.1 \pm 0.6$ | – | – |
| $Z \to \mu\mu$ | $89.0 \pm 0.7$ | $4.3 \pm 0.1$ | – | – | $373582 \pm 275$ | $1247 \pm 6$ |
| $Z \to \tau\tau$ | $3870.8 \pm 7.2$ | $7.1 \pm 0.1$ | $1440.9 \pm 3.5$ | $0.67 \pm 0.04$ | $2659 \pm 27.7$ | $12 \pm 0.7$ |
| $t\bar{t}$ | $311.9 \pm 0.2$ | $93.8 \pm 0.1$ | $159.0 \pm 0.2$ | $47.0 \pm 0.1$ | $183.9 \pm 0.7$ | $74.6 \pm 0.4$ |
| $W + jets/\gamma$ | $266.9 \pm 4.7$ | $112.2 \pm 3.4$ | $307.6 \pm 5.1$ | $122.2 \pm 3.5$ | $235.5 \pm 3.5$ | $91.5 \pm 2.2$ |
| $WW$ | $454.7 \pm 0.1$ | $164.5 \pm 0.1$ | $202.4 \pm 0.12$ | $73.9 \pm 0.07$ | $272.1 \pm 0.6$ | $107.3 \pm 0.3$ |
| $WZ$ | $23.6 \pm 0.1$ | $7.6 \pm 0.1$ | $136.9 \pm 0.03$ | $11.5 \pm 0.01$ | $171.4 \pm 0.1$ | $21.5 \pm 0.04$ |
| $ZZ$ | $5.4 \pm 0.01$ | $0.6 \pm 0.01$ | $116.9 \pm 0.01$ | $9.3 \pm 0.01$ | $147.2 \pm 0.05$ | $18.0 \pm 0.02$ |
| Multi-jet | $430.4 \pm 20.7$ | $6.4 \pm 2.5$ | $1370 \pm 11$ | $1.0 \pm 0.3$ | $408 \pm 29$ | $53.8 \pm 9.7$ |
| Signal ($M_H = 160$ GeV) | $18.8 \pm 0.2$ | $13.5 \pm 0.1$ | $11.2 \pm 0.01$ | $7.21 \pm 0.01$ | $13.4 \pm 0.2$ | $9.03 \pm 0.1$ |
| Total Background | $5572.3 \pm 22.5$ | $396.5 \pm 4.2$ | $278619 \pm 106$ | $424 \pm 3.6$ | $377661 \pm 277$ | $1626 \pm 11$ |
| Data | 5566 | 390 | 278277 | 421 | 384083 | 1613 |

TABLE II: Expected and observed number of events in each channel after pre-selection and final selections (the NN input stage). Statistical uncertainties in the expected yields are shown for all backgrounds whereas the systematic uncertainty is shown for the multijet background.

| **NN Analysis Variables** | |
|---|---|
| $p_T$ of leading lepton | $p_T(\ell_1)$ |
| $p_T$ of trailing lepton | $p_T(\ell_2)$ |
| Lepton quality ranking | $\min(q_{\ell 1}, q_{\ell 2})$ |
| Vector sum of the transverse momenta of the leptons: | $\vec{p}_T^{\,1} + \vec{p}_T^{\,2}$ |
| Scalar sum of the transverse momenta of the jets: | $H_T = \sum_i p_T(\text{jet}_i)$ |
| Invariant mass of both leptons | $M_{\text{inv}}(\ell_1, \ell_2)$ |
| Minimal transverse mass of one lepton and $\not\!\!E_T$ | $M_T^{min}$ |
| Missing transverse energy | $\not\!\!E_T$ |
| Azimuthal angle between selected leptons | $\Delta\phi(\ell_1, \ell_2)$ |
| Azimuthal angle between leading lepton and $\not\!\!E_T$ | $\Delta\phi(\not\!\!E_T, \ell_1)$ |
| Azimuthal angle between trailing lepton and $\not\!\!E_T$ | $\Delta\phi(\not\!\!E_T, \ell_2)$ |
| Jet multiplicity | $n_{jet}$ |

TABLE III: Input variables for the NN.

## VI. RESULTS AND SUMMARY

The estimates for the expected number of background and signal events depend on numerous factors that each introduce an associated systematic uncertainty. We consider the effect of systematic uncertainties both on the normalization and on the shape of the neural network's differential distributions for signal and backgrounds. The following sources of systematic uncertainties affecting only the normalization of the backgrounds and of the signal efficiency have been considered: lepton reconstruction efficiencies (2.5-4%), lepton momentum calibration (2-8%), theoretical cross section (diboson 7%, $t\bar{t}$ 10%, $W$+jet 6%, $Z$+jet 6%) Higgs signal PDFs (8%) and modeling of multijet background (2-20%), luminosity (6.1%). For the following source of systematic uncertainties we consider also the impact on the shape the NN distributions: jet reconstruction efficiency (6-18%), jet energy scale calibration (3-17%), jet energy resolution (2%), modeling of $p_{\rm T}(WW)$, $p_{\rm T}(H)$, and $p_{\rm T}(Z)$ (1-5%). A change of the $p_{\rm T}(WW)$ spectrum leads as well to a change of the $\Delta\phi(\ell,\ell)$ distribution. The systematic uncertainty on the $W$ and $Z$ boson $p_{\rm T}$ modeling is determined by comparing the $p_{\rm T}$ distributions of PYTHIA to the measured $p_{\rm T}$ distributions in data. The total uncertainty on the background level is approximately 10% and for the signal efficiency it is 13%.

After all selection cuts, the NN output distributions in data agree within uncertainties with the expected backgrounds as shown in Figure 2. Thus the NN output distributions are used to set limits on the Higgs boson inclusive production cross section $\sigma(p\overline{p} \to H + X)$ assuming SM values for the branching ratios. We calculate limits for each channel and all three channels combined, using a modified frequentist method, the CLs method, with a log-likelihood ratio (LLR) test statistic [25]. To minimize the degrading effects of systematics on the search sensitivity, the individual background contributions are fitted to the data observation by maximizing a profile likelihood function for each hypothesis [26].

Table IV presents expected and observed upper limits at 95% C.L. for $\sigma(p\overline{p} \to H + X)$ relative to that expected in the SM for each of the three final states and for their combination for each Higgs boson mass considered. Figure 3 shows Data and SM signal expectation after background subtraction as a function of the neural net output variable. The background resulting from the constrained fit using the signal plus background hypothesis is subtracted.

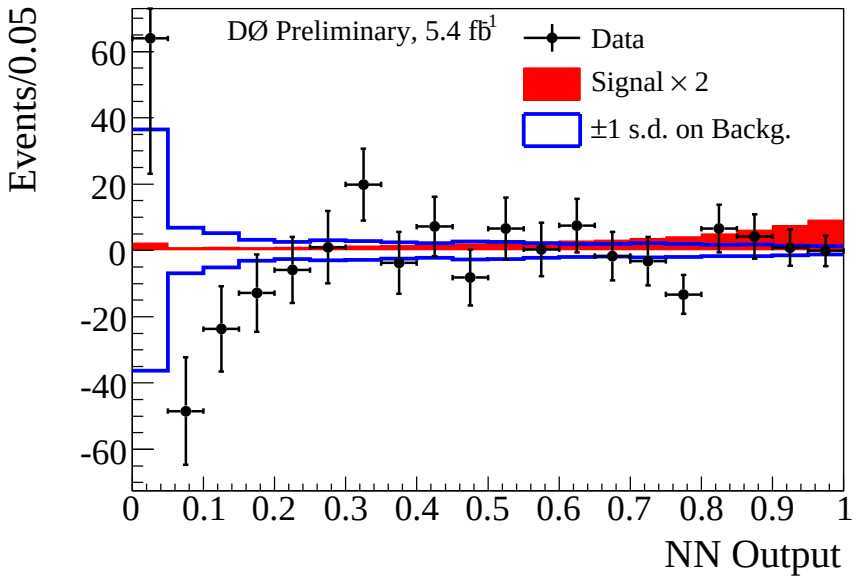


FIG. 3: Data and SM signal expectation after background subtraction as a function of the neural net output variable. The background resulting from the constrained fit using the signal plus background hypothesis is subtracted. The standard model signal expectation is shown by the red histogram. The constrained total systematic uncertainty is shown by the blue line. The signal expectations corresponds to a $m_{\rm h}$mass of 165 GeV. 5.4 fb$^{-1}$ of Run II data.

Figure 5 shows the expected and observed limits for $\sigma(p\overline{p} \to H + X)$ relative to the SM for the different Higgs boson masses and the LLR distribution for the 5.4 fb$^{-1}$ of Run II data. Figure 6 shows the confidence level for the exclusion of the cross section $\sigma(p\overline{p} \to H + X)$ in units of the SM cross section for all the three channels combined as a function of the Higgs boson mass.

TABLE IV: Expected and observed upper limits at 95% C.L. for $\sigma(p\overline{p} \to H + X)$ relative to the SM for $e^+e^-$, $e\mu$, and $\mu^+\mu^-$ final states in Run II and their combination for different Higgs boson masses ($M_H$).

| $M_H$= | 115 | 120 | 125 | 130 | 135 | 140 | 145 | 150 | 155 | 160 | 165 | 170 | 175 | 180 | 185 | 190 | 195 | 200 |
|---|---|---|---|---|---|---|---|---|---|---|---|---|---|---|---|---|---|---|
| $ee$ (exp.) | 47.98 | 29.98 | 19.15 | 13.43 | 9.24 | 7.76 | 6.30 | 5.14 | 4.25 | 3.15 | 3.05 | 3.64 | 4.16 | 5.33 | 6.63 | 8.45 | 10.30 | 12.28 |
| $ee$ (obs.) | 60.81 | 27.76 | 20.68 | 16.17 | 12.16 | 11.17 | 8.64 | 8.09 | 6.85 | 4.10 | 3.64 | 4.31 | 5.28 | 5.50 | 6.12 | 9.00 | 11.41 | 14.14 |
| $e\mu$ (exp.) | 24.19 | 16.48 | 12.25 | 8.95 | 6.92 | 5.54 | 5.00 | 4.14 | 3.16 | 2.17 | 1.93 | 2.30 | 2.84 | 3.53 | 4.28 | 5.26 | 6.22 | 7.44 |
| $e\mu$ (obs.) | 31.59 | 21.33 | 15.41 | 10.77 | 8.02 | 6.27 | 4.26 | 3.51 | 3.74 | 2.41 | 1.99 | 2.48 | 2.29 | 2.36 | 4.50 | 3.91 | 6.39 | 6.29 |
| $\mu\mu$ (exp.) | 28.13 | 18.49 | 12.15 | 9.25 | 7.31 | 6.30 | 5.39 | 4.68 | 3.88 | 3.08 | 2.94 | 3.40 | 4.07 | 4.77 | 6.27 | 7.85 | 9.41 | 11.76 |
| $\mu\mu$ (obs.) | 37.55 | 23.11 | 15.55 | 9.58 | 9.64 | 7.51 | 7.76 | 5.65 | 5.45 | 2.95 | 2.83 | 3.09 | 3.80 | 4.90 | 5.82 | 8.21 | 9.83 | 12.72 |
| Run II (exp.) | 14.88 | 9.74 | 7.20 | 5.40 | 4.23 | 3.48 | 3.07 | 2.58 | 2.02 | 1.43 | 1.36 | 1.65 | 2.06 | 2.59 | 3.28 | 4.20 | 5.08 | 6.23 |
| Run II (obs.) | 20.78 | 13.60 | 8.81 | 6.63 | 6.41 | 5.21 | 3.94 | 3.29 | 3.25 | 1.82 | 1.55 | 1.96 | 1.89 | 2.11 | 3.17 | 3.27 | 5.77 | 5.53 |

When integrating distributions for $\log_{10}(s/b)$ from the high-$s/b$ side downwards one obtains Fig. 4. This plot shows the sums of signal, background, and data of all three channels added together.

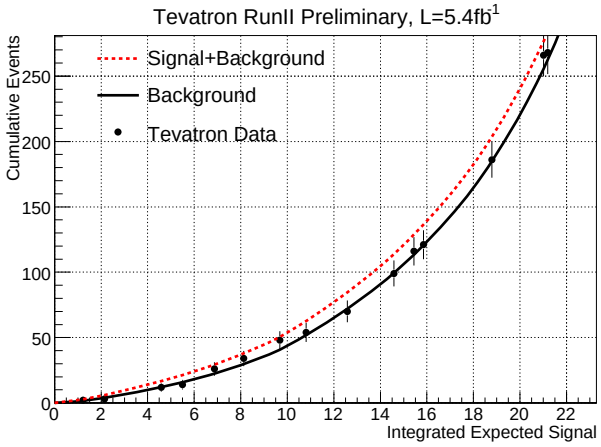


FIG. 4: Integrated distributions of $s/b$, starting at the high $s/b$ side. The total signal+background and background-only integrals are shown separately, along with the data sums. Data are only shown for bins that have data events in them. The Signal expectation corrsponds to a Higgs boson mass of $M_H$=165 GeV.

An improvement of 15-20% is seen in the expected limits in the most sensitive region compared to the previous result [6]. This improvements come from additional data, improved separation power of the multivariate methods and considering higher jet multiplicities in the $\mu\mu$ final state. Furthermore, the agreement between the expected and observed limits has improved with the refinements in the background model. So far, no region of the SM Higgs boson mass range can be excluded and no significant excess of events is observed in data. However using the data of DØ alone the sensitivity of the current analysis has reached an expected confidence level for the exclusion of the SM cross section for an Higgs boson with $M_H \approx 165$ GeV over 85%. With increased integrated luminosity it will be possible to exclude the presence of a Higgs boson with masses in this range.


[1] R. Barate *et al.*, Phys. Lett. B **565**, 61 (2003).
[2] The LEP Electroweak Working Group, the Tevatron Electroweak Working Group, *Precision Electroweak Measurements and Constraints on the Standard Model*, `http://lepewwg.web.cern.ch/LEPEWWG/plots/summer2009/`
[3] T. Han, A. Turcot, R-J. Zhang, Phys. Rev. D **59**, 093001 (1999).
[4] M. Carena *et al.* [Higgs Working Group Collaboration], "Report of the Tevatron Higgs working group", hep-ph/0010338.
[5] V. Abazov *et al.*, DØ Collaboration, Phys. Rev. Lett. **96**, 011801 (2006).

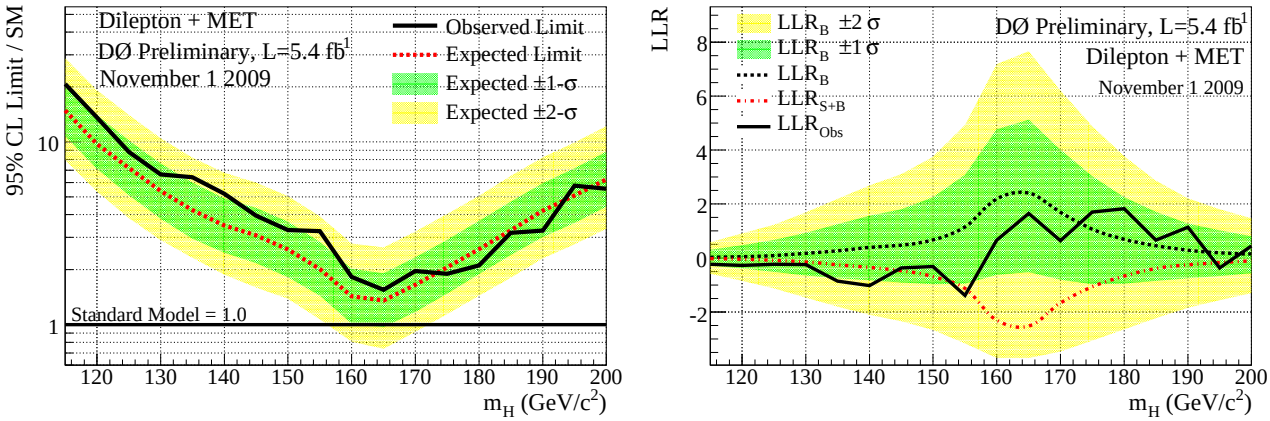


FIG. 5: Excluded cross section ($\sigma(p\overline{p} \to H + X)$) at 95% C.L. in units of the SM cross section (left) and LLR (right) for all three channels combined as a function of the Higgs boson mass, using 5.4 fb$^{-1}$ of Run II data.

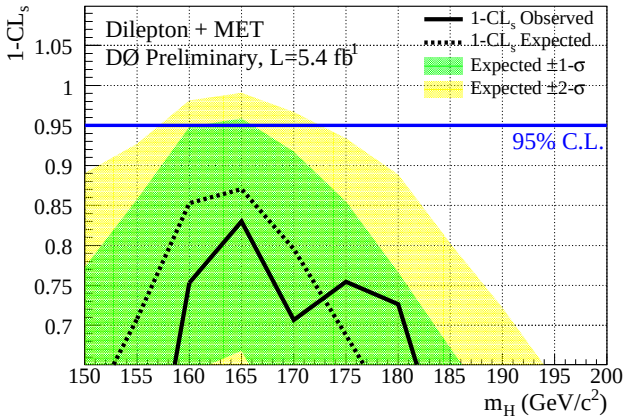


FIG. 6: Confidence level for the exclusion of the cross section $\sigma(p\overline{p} \to H + X)$ in units of the SM cross section for all the three channels combined as a function of the Higgs boson mass, using 5.4 fb$^{-1}$ of Run II data.


[6] DØ Collaboration, *Search for the Higgs Boson in $H \to WW^{(*)} \to \ell\ell'$ ($\ell, \ell' = e, \mu$) decays with 3.0–4.2 $fb^{-1}$ of $p\overline{p}$ Collisions at $\sqrt{s} = 1.96$ TeV*, DØNote 5871, (March 2009).
[7] DØ Collaboration, V. Abazov *et al.*, Nucl. Instrum. Methods Phys. Res. A. **565**, 463 (2006).
[8] T. Andeen *et al.*, FERMILAB–TM–2365 (2007).
[9] T. Sjöstrand *et al.*, Comp. Phys. Comm. **135**, 238 (2001), we use version 6.323 or later.
[10] M.L. Mangano, M. Moretti, F. Piccinini, R. Pittau, A. Polosa, JHEP **0307**, 001 (2003), we use version 2.11.
[11] J. Pumplin et al., JHEP **07**, 012 (2002).
[12] R. Brun and F. Carminati, CERN Program Library Long Writeup W5013, 1993 (unpublished).
[13] S. Catani, D. de Florian, M. Grazzini and P. Nason, JHEP **0307**, 028 (2003).
[14] K.A. Assamagan *et al.*, [Higgs Working Group Collaboration], arXiv:hep-ph/0406152.
[15] U. Aglietti, R. Bonciani, G. Degrassi, A. Vicini, arXiv:hep-ph/0610033.
[16] C. Anastasiou, R. Boughezal, F. Petriello, arXiv:0811.3458 [hep-ph].
[17] S. Frixione and B.R. Webber, JHEP **0206**, 029 (2002).
[18] T. Gleisberg, S. Höche, F. Krauss, A. Schälicke, S. Schumann and J. Winter, JHEP **0402**, 056 (2004).
[19] R. Hamberg, W.L. van Neerven, and T. Matsuura, Nucl. Phys. **B359**, 343 (1991) [Erratum-ibid. **B644**, 403 (2002)].
[20] V. Abazov *et al.*, DØ Collaboration, Phys. Rev. Lett. **100**, 102002 (2008)
[21] K. Melnikov and F. Petriello, Phys. Rev. D **74**, 114017 (2006).
[22] S. Moch, P. Uwer, Phys. Rev. D**78**, 034003 (2008), we use $\sigma(t\overline{t}) = 7.88$ pb.
[23] J. M. Campbell and R. K. Ellis, Phys. Rev. D **60**, 113006 (1999), we use $\sigma(WW) = 11.66$ pb, $\sigma(WZ) = 3.45$ pb and $\sigma(ZZ) = 1.37$ pb.
[24] T. Binoth, M. Ciccoli, N. Kauer and M. Krämer, JHEP **0503**, 065 (2005); JHEP **0612**, 046 (2006).
[25] T. Junk, Nucl. Instrum. Methods Phys. Res. A. **434**, 435 (1999). A. Read, CERN 2000-005 (30 May 2000).

[26] W. Fisher, FERMILAB-TM-2386-E.

## APPENDIX A: ADDITIONAL PLOTS

### 1. $e^+e^-$ Marginal

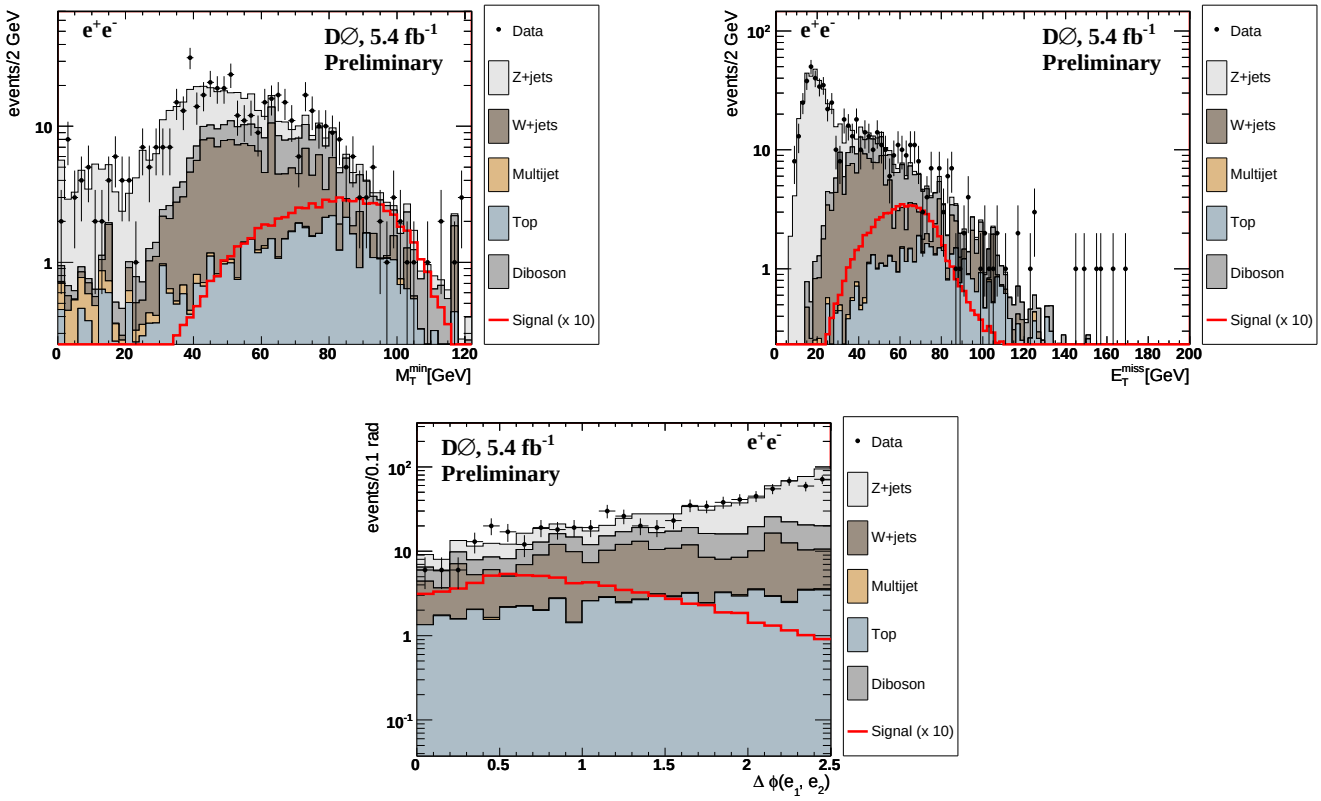


FIG. 7: Distributions of $\not\!\!E_T$ (a), minimum $M_T$ (b), and $\Delta\phi(e^+, e^-)$ (d) for data (points with error bars), background simulation (histograms, complemented with the QCD expectation) and signal expectation times 10 for $M_H = 165$ GeV (solid line) for the $e^+e^-$ channel after full selection but excluded the cut of the plotted variable.

### 2. $e^+e^-$ Preselection

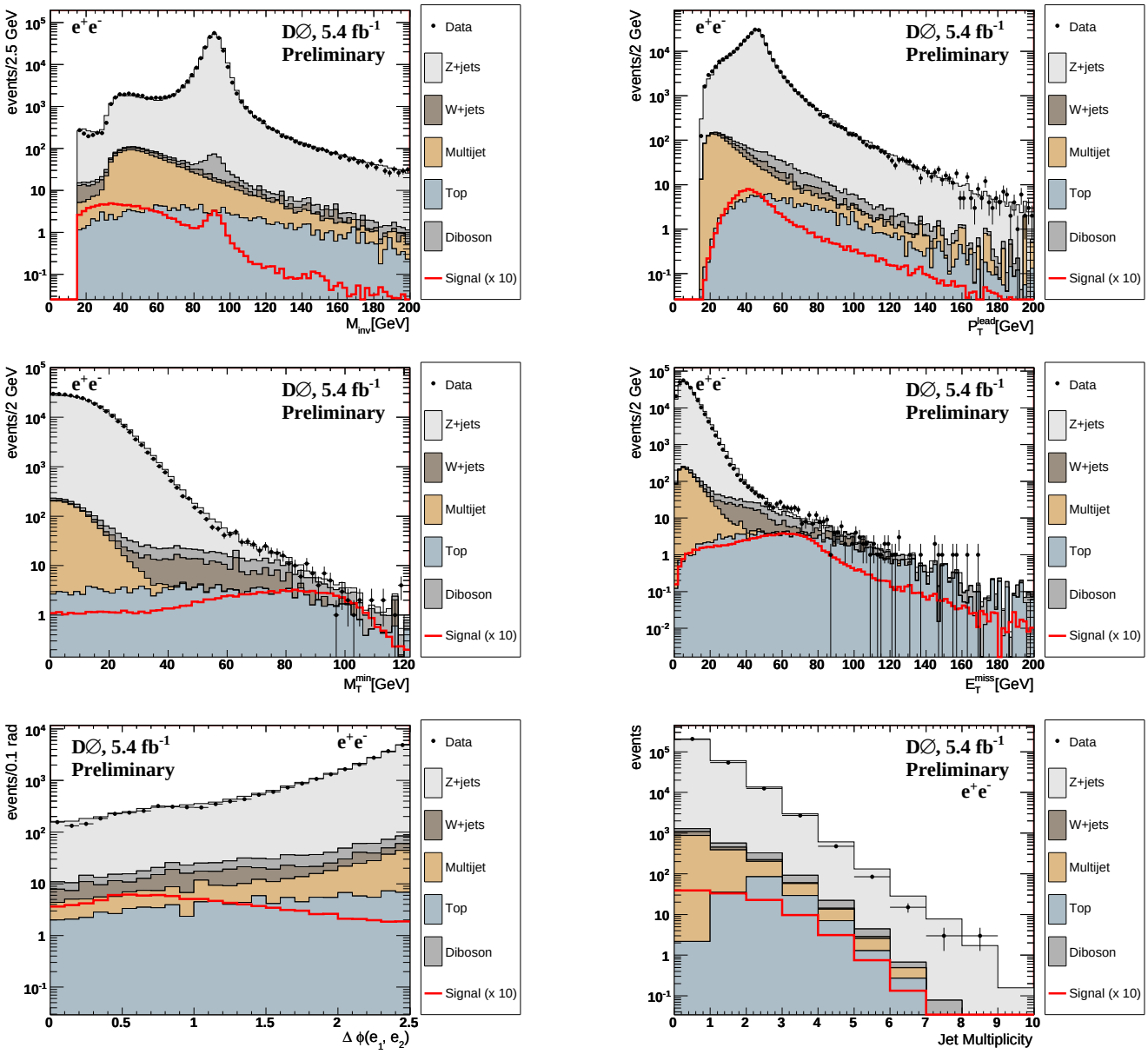


FIG. 8: Distributions of $\ell^+\ell^-$ mass (a), leading electron $p_T$ (b), $\not\!\!E_T$ (c), minimum $M_T$ (d), $\Delta\phi(e^+, e^-)$ (e), and jet multiplicity (f) for data (points with error bars), background simulation (histograms, complemented with the QCD expectation) and signal expectation times 10 for $M_H = 165$ GeV (solid line) for the $e^+e^-$ channel after preselection.

### 3. $e\mu$ Marginal

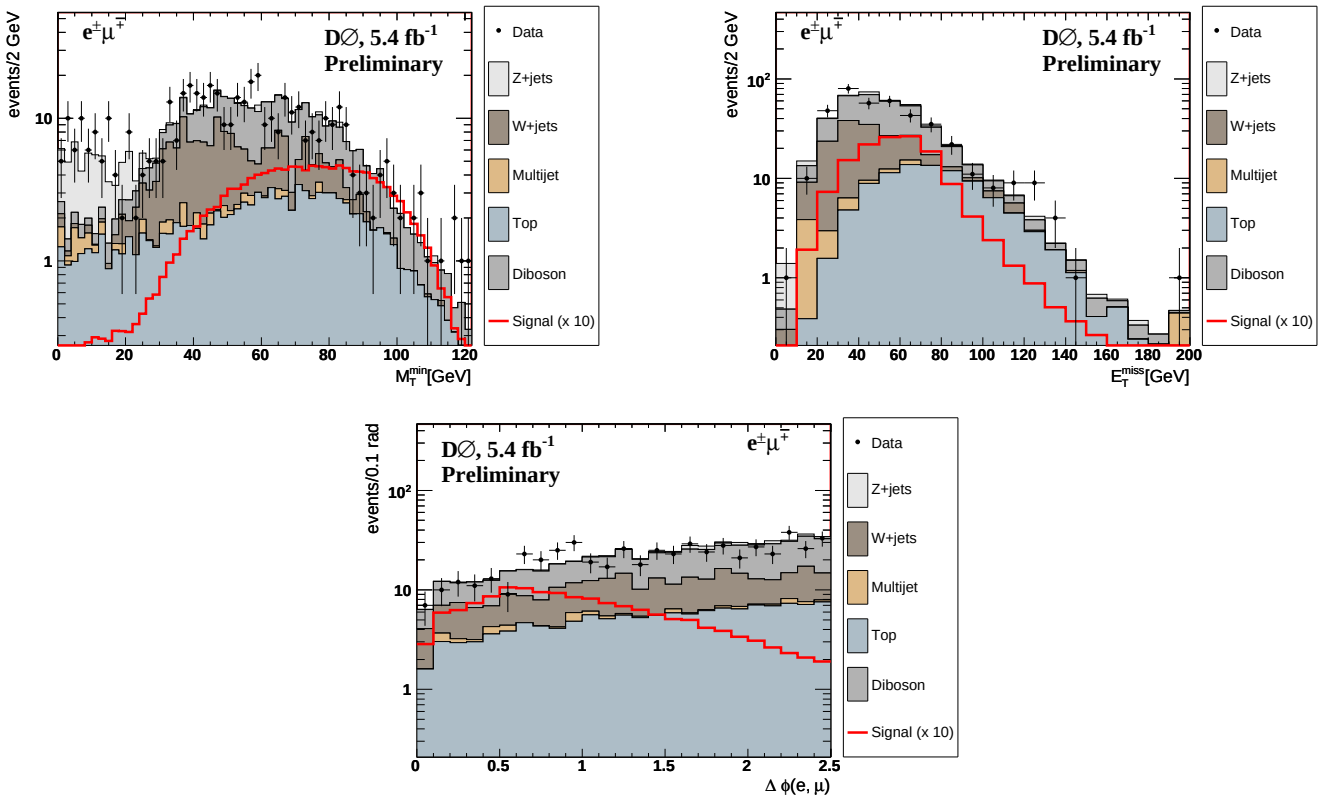


FIG. 9: Distributions of $\not\!\!E_T$ (a), minimum $M_T$ (b), and $\Delta\phi(e,\mu)$ (d) for data (points with error bars), background simulation (histograms, complemented with the QCD expectation) and signal expectation times 10 for $M_H = 165$ GeV (solid line) for the $e\mu$ channel after full selection but excluded the cut of the plotted variable.

### 4. $e\mu$ Preselection

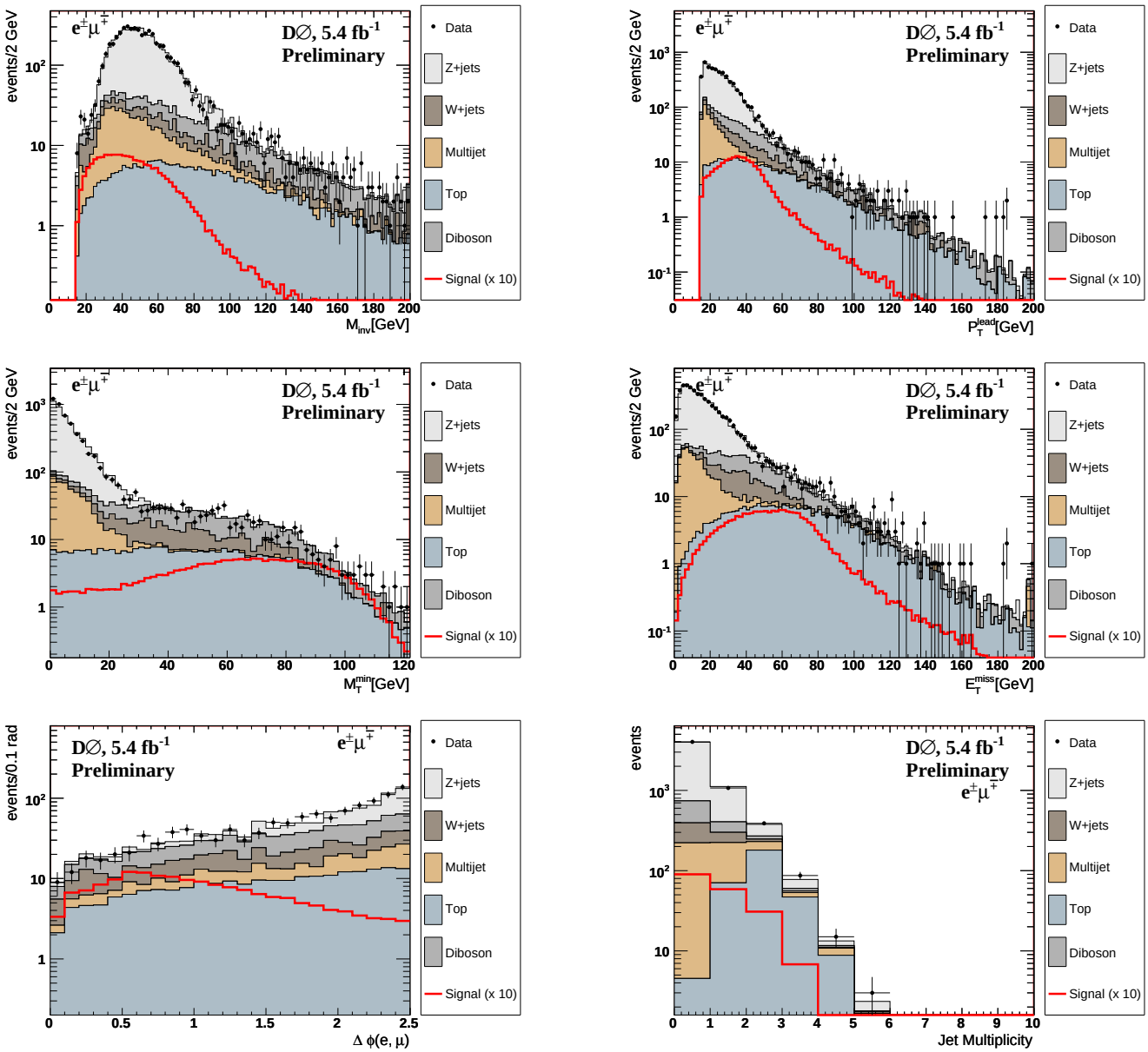


FIG. 10: Distributions of $\ell^+\ell^-$ mass (a), leading lepton $p_T$ (b), $\not\!\!E_T$ (c), minimum $M_T$ (d), $\Delta\phi(e,\mu)$ (e), and jet multiplicity (f) for data (points with error bars), background simulation (histograms, complemented with the QCD expectation) and signal expectation times 10 for $M_H = 165$ GeV (solid line) for the $e\mu$ channel after preselection.

### 5. $\mu\mu$ Marginal

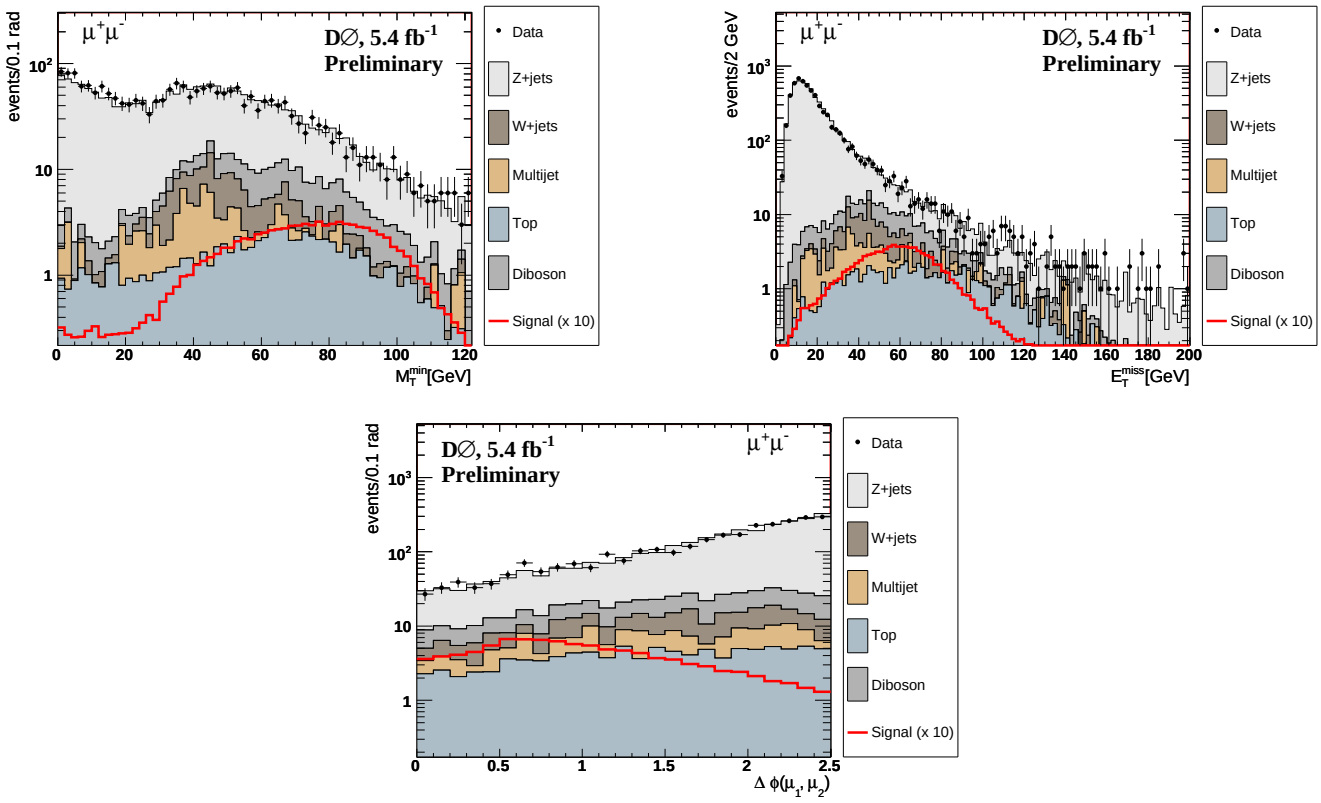


FIG. 11: Distributions of $\not\!\!E_T$ (a), minimum $M_T$ (b), and $\Delta\phi(\mu^+,\mu^-)$ (d) for data (points with error bars), background simulation (histograms, complemented with the QCD expectation) and signal expectation times 10 for $M_H = 165$ GeV (solid line) for the $\mu\mu$ channel after full selection but excluded the cut of the plotted variable.

### 6. $\mu^+\mu^-$ Preselection

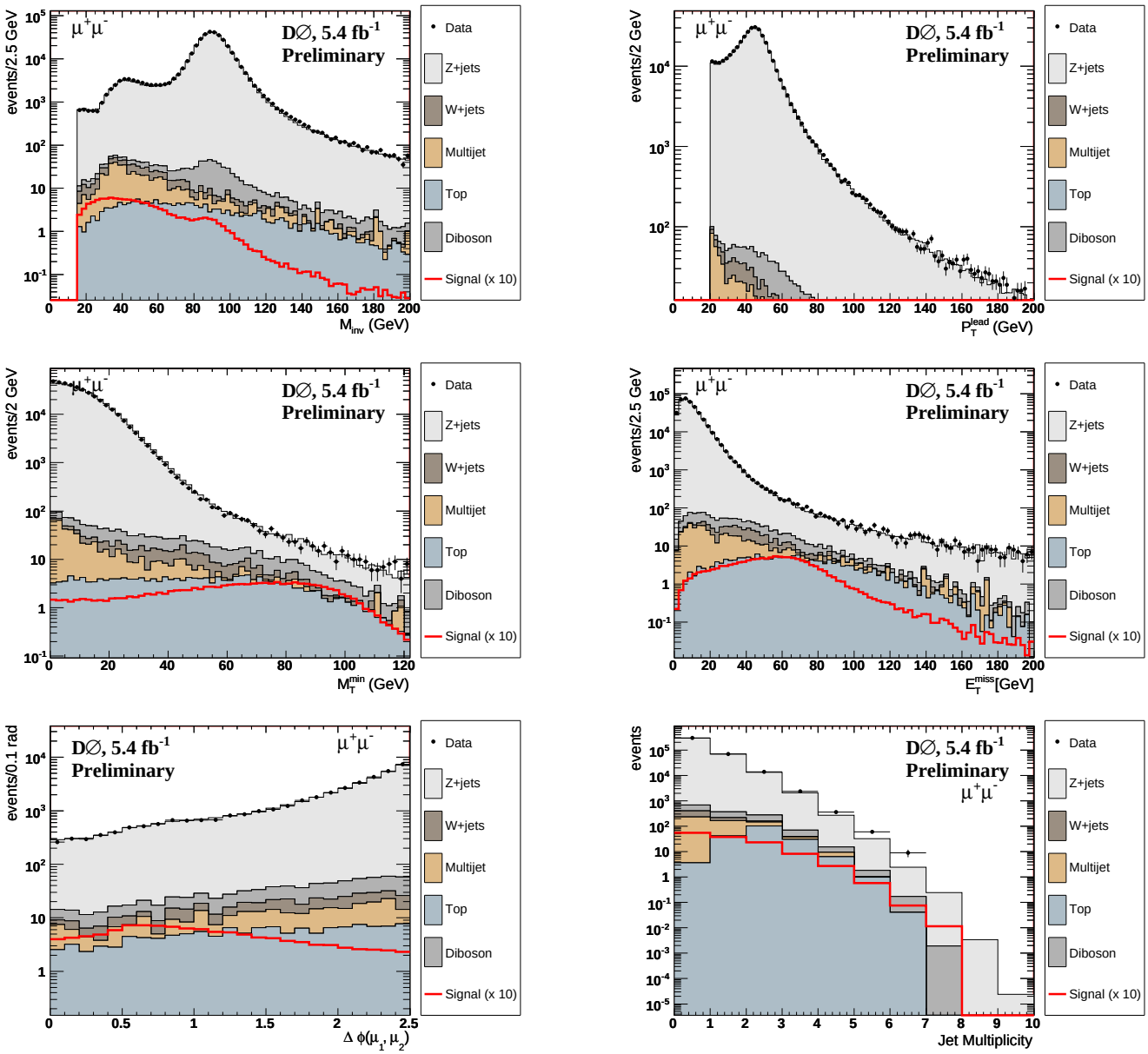


FIG. 12: Distributions of $\ell^+\ell^-$ mass (a), leading lepton $p_T$ (b), $\not\!\!E_T$ (c), minimum $M_T$ (d), $\Delta\phi(e,\mu)$ (e), and jet multiplicity (f) for data (points with error bars), background simulation (histograms, complemented with the QCD expectation) and signal expectation times 10 for $M_H = 165$ GeV (solid line) for the $\mu^+\mu^-$ channel after preselection.

## 7. $e^+e^-$ Final Selection

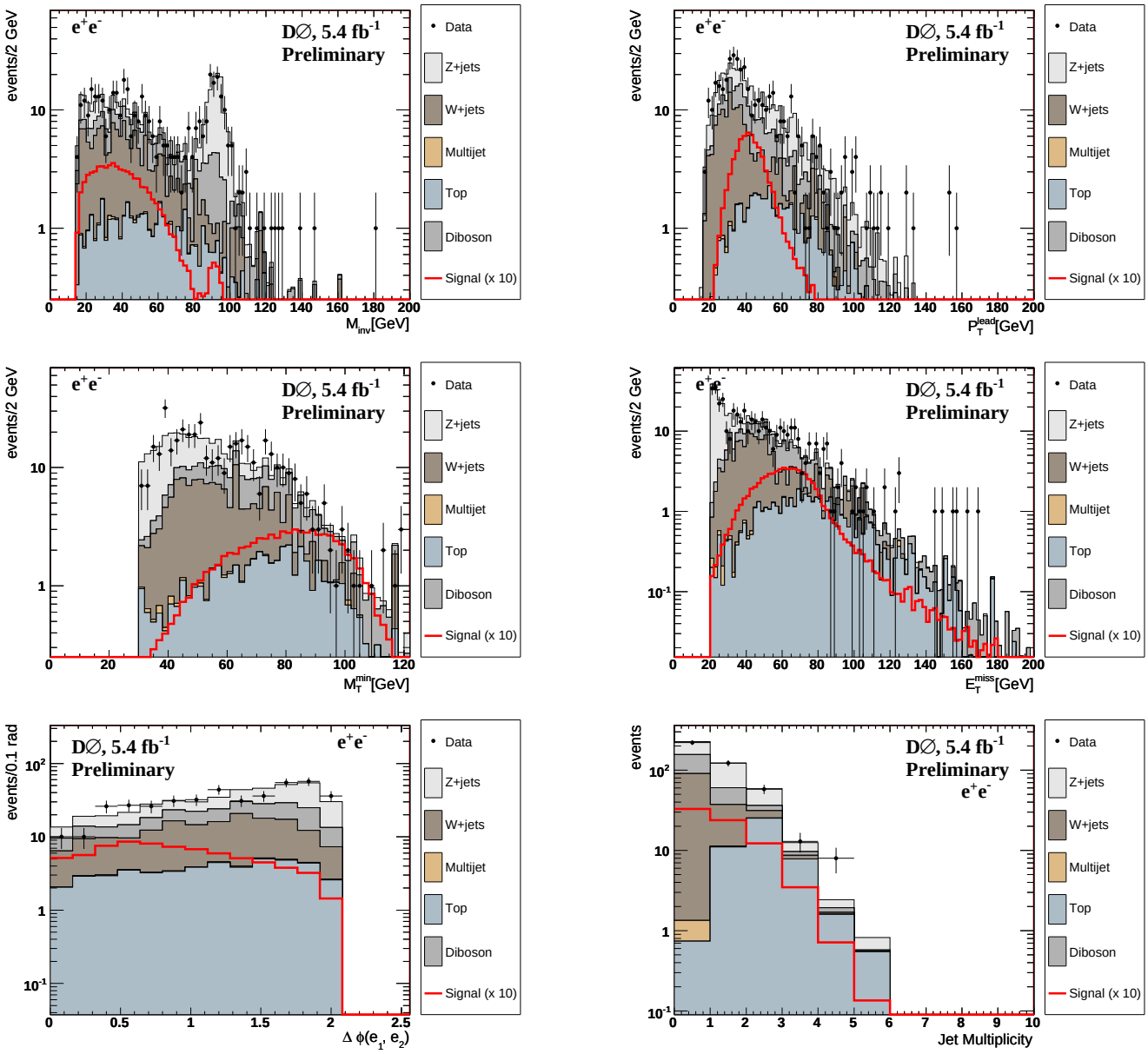


FIG. 13: Distributions of $\ell^+\ell^-$ mass (a), leading electron $p_T$ (b), $\not\!\!E_T$ (c), minimum $M_T$ (d), $\Delta\phi(e^+, e^-)$ (e), and jet multiplicity (f) for data (points with error bars), background simulation (histograms, complemented with the QCD expectation) and signal expectation times 10 for $M_H = 165$ GeV (solid line) for the $e^+e^-$ channel after final selection.

## 8. $e\mu$ Final Selection

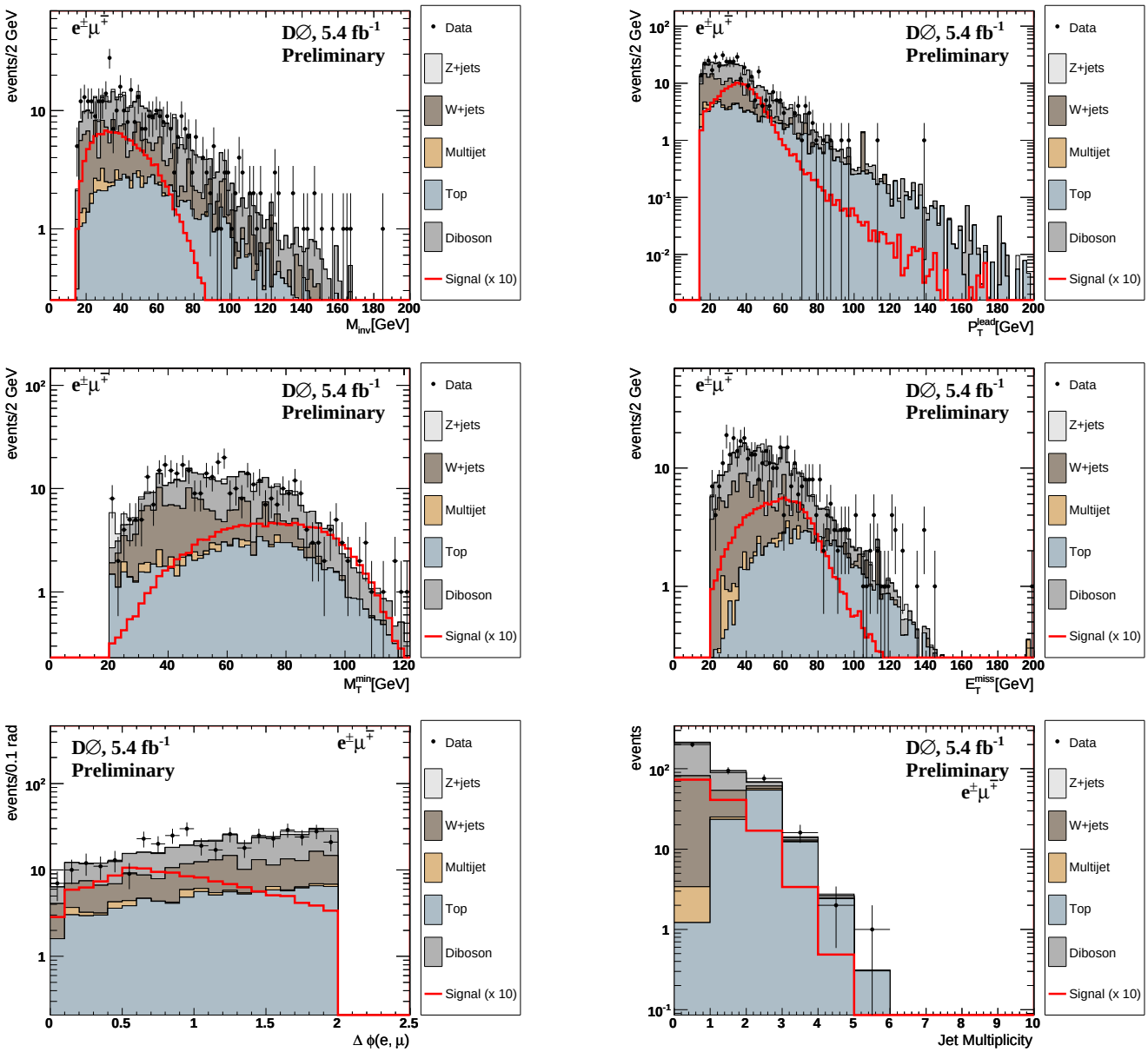


FIG. 14: Distributions of $\ell^+\ell^-$ mass (a), leading lepton $p_T$ (b), $\not\!\!E_T$ (c), minimum $M_T$ (d), $\Delta\phi(e,\mu)$ (e), and jet multiplicity (f) for data (points with error bars), background simulation (histograms, complemented with the QCD expectation) and signal expectation times 10 for $M_H = 165$ GeV (solid line) for the $e\mu$ channel after final selection.

## 9. $\mu^+\mu^-$ Final Selection

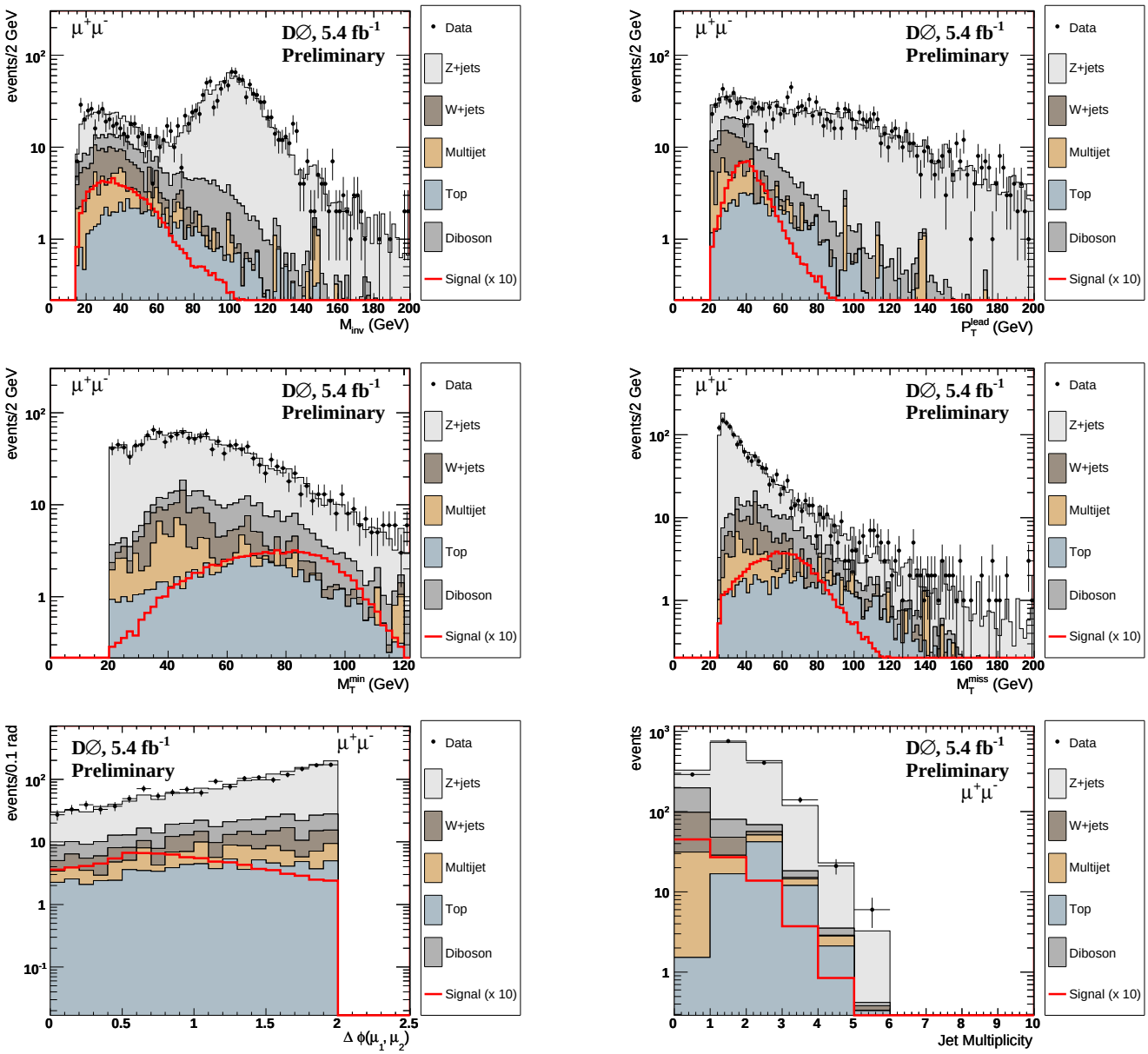


FIG. 15: Distributions of $\ell^+\ell^-$ mass (a), leading lepton $p_T$ (b), $\not\!\!E_T$ (c), minimum $M_T$ (d), $\Delta\phi(e,\mu)$ (e), and jet multiplicity (f) for data (points with error bars), background simulation (histograms, complemented with the QCD expectation) and signal expectation times 10 for $M_H = 165$ GeV (solid line) for the $\mu^+\mu^-$ channel after final selection.